AMMA dust experiment : an overview of measurements performed during the dry season special observation period (SOP0) at the Banizoumbou (Niger) supersite - art. no. D00C14

Jean Louis Rajot, P. Formenti, Stéphane Alfaro, Karine Desboeufs, Servanne Chevaillier, Bernadette Chatenet, A. Gaudichet, Emilie Journet, Beatrice Marticorena, Sylvain Triquet, et al.

AMMA dust experiment: An overview of measurements performed during the dry season special observation period (SOP0) at the Banizoumbou (Niger) supersite

Jean Louis Rajot,[1] Paola Formenti,[2] Stéphane Alfaro,[2] Karine Desboeufs,[2] Servanne Chevaillier,[2] Bernadette Chatenet,[1,2] Annie Gaudichet,[2] Emilie Journet,[2] Béatrice Marticorena,[2] Sylvain Triquet,[2] Aliko Maman,[1] Nicolas Mouget,[1] and Alfari Zakou[1]

Received 1 February 2008; revised 16 June 2008; accepted 11 July 2008; published 30 October 2008.

[1] In the frame of the African Monsoon Multidisciplinary Analysis–Special Observation Period 0 (AMMA SOP0) field campaign, a sophisticated instrumental setup specially designed for documenting the characteristics of aerosols in the surface boundary layer has been operated for 1 month (13 January to 13 February 2006) at the Banizoumbou supersite in Niger. The analysis of the long-term routine sunphotometer measurements shows that the intensive measurements were performed during a transition phase between a period when biomass burning aerosols are present in the atmospheric column and another when mineral dust is clearly predominant. On the basis of ground-level observations, three types of events can be defined. (1) Type B events are those corresponding to advection of Biomass burning plumes from southern Sahel. They represent only 3% of the measurement period. (2) Type D events are those during which mineral dust concentrations are larger than 200 μg m^{-3}. They represent 35% of the measuring time, and coincide with advection of mineral dust from distant sources to the measurement site. The composition of the dust differs significantly from one episode to the other, depending on the trajectory of air mass that transported it. (3) Type L events are those that can be explained by occurrence of local erosion and that are of short duration. During them, the aerosol size distribution is dominated by a coarser mode (9 μm) than during the events of the D type dominated by a finer mode (4.5 μm). Elemental analysis also shows that mineral dust is relatively rich in Fe and poor in Ca, which is typical of the Sahelian aerosols.

Citation: Rajot, J. L., et al. (2008), AMMA dust experiment: An overview of measurements performed during the dry season special observation period (SOP0) at the Banizoumbou (Niger) supersite, *J. Geophys. Res.*, *113*, D00C14, doi:10.1029/2008JD009906.

1. Introduction

[2] Both the most recent reports of the *Intergovernmental Panel on Climate Change* [2001, 2007] highlight the uncertainties that still affect the estimate of the contribution of mineral dust to radiative forcing. These are due to a poor knowledge of the concentration field and physicochemical properties of mineral dust.

[3] Three major research tools have been used to investigate these uncertainties: aircraft campaigns, remote sensing, and modeling studies [*Washington et al.*, 2006]. These authors also warn on the rarity of ground-based field campaigns, particularly in the vicinity of source areas. To be representative of the overall aerosol content in the atmosphere, ground-based campaigns must be coupled with vertically resolved and/or vertically integrated measurements.

[4] Nevertheless, ground-based studies are absolutely necessary to study the impact of mineral dust on health [e.g., *Thomson et al.*, 2006] and on soil fertility [*Swap et al.*, 1992; *Valentin et al.*, 2004]. They are also essential to constrain the models describing the mineral dust cycle, in particular their emission and deposition modules [*Gomes et al.*, 2003; *Alfaro et al.*, 2004; *Goossens and Rajot*, 2008].

[5] Since the early work of *Schütz et al.* [1981], the Sahara has been recognized as the "world's largest source of aeolian soil dust" [*Goudie and Middleton*, 2001]. To date, it is estimated that the Sahara emits up to 670 Mt per year [*Laurent*, 2005]. Regarding the contribution of the Sahel to dust emission, it is currently debated [*Engelstaedter and Washington*, 2006], but it might become more important in the future owing to the increasing population of the area [*Guengant and Banoin*, 2003;

[1]Institut de Recherche pour le Developpement, UR176, Niamey, Niger.
[2]Laboratoire Interuniversitaire des Systèmes Atmosphériques, Universités Paris 12 Val de Marne et Paris 7-Denis Diderot, CNRS, Créteil, France.

0148-0227/08/2008JD009906

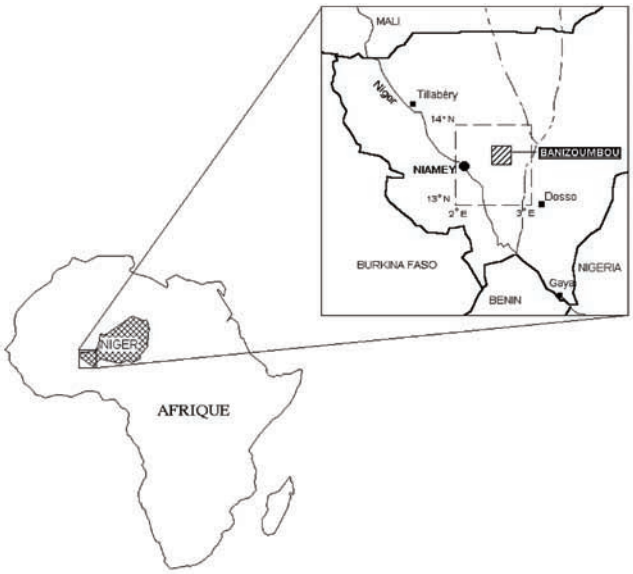

Figure 1. Location of the experimental site of Banizoumbou.

Leblanc et al., 2008]. In this case, dust emitted from the Sahel could be considered as being of anthropogenic origin, and should therefore be accounted for when estimating the global radiative forcing of the Earth-atmosphere system.

[6] In wintertime, forest fires for land clearing are commonplace in the southern part of the Sahel that is a major source of biomass burning aerosols. These aerosols are expected to mix with mineral dust that is transported southward toward the Gulf of Guinea by trade winds.

[7] The first field phase of the African Monsoon Multidisciplinary Analysis (AMMA SOP0/DABEX–Dust And Biomass burning EXperiment) has been dedicated to the study of mineral dust, biomass burning aerosols, and their mixing [*Redelsperger et al.*, 2006; *Haywood et al.*, 2008]. In this framework, several ground-based supersites were operated in Niger, Benin and Senegal during the January–February, 2006 period. The Facility for Airborne Atmospheric Measurements (FAAM) BAe-146 was also operated from Niamey, in Niger [*Haywood et al.*, 2008].

[8] In this paper, we present results from the ground-based measurements of aerosol concentrations and physicochemical properties which were conducted at the AMMA supersite of Banizoumbou, in Niger, from 13 January to 13 February 2006.

[9] First, this paper aims at presenting the field installation, which was designed specially for AMMA in order to take into account the experimental challenges in investigating mineral dust, in particular the sampling of particles larger than 1 μm diameter. Measurements will be discussed to illustrate the general situation of the SOP0 period in terms of meteorological conditions and aerosol type and atmospheric load. The occurrence of specific episodes of intrusion of mineral dust and biomass burning aerosols which were advected at the site will also be illustrated. These episodes will be characterized in terms of their origin, aerosol composition and size distribution.

[10] This paper completes the body of observations on mineral dust source and properties also presented in this special issue of JGR [*Formenti et al.*, 2008; *Chou et al.*, 2008; *Osborne et al.*, 2008].

2. Experimental Setup

[11] The AMMA super site of Banizoumbou (13.5°N 2.6°E, 250 m above sea level), is located at a remote location at about 60 km east from the capital of Niger, Niamey (Figure 1). This site has been operational since the early 1990s, when the first measurements of soil erosion were performed on a cultivated field and a fallow [*Rajot et al.*, 1995; *Rajot*, 2001]. Since 1995, the site is also an Aerosol Robotic Network (AERONET) station measuring columnar aerosol optical properties.

[12] Two novel sampling stations were implemented in the framework of AMMA (Figure 2). The first one aims at monitoring the aerosol dynamics at the seasonal and interannual timescales (AMMA EOP). It consists of measurements of surface PM_{10} mass concentrations and total deposition, as well as measurements of the aerosol vertical profile twice a day.

[13] The second station is designed for intensive measurements (AMMA SOP). It consisted into an instrumented container sampling from two wind-oriented multiline inlets. The container was buried underground in order to avoid disturbances in the airflow. Full details are presented in the following paragraphs. A laboratory was also set up as a clean room where aerosol samples were prepared, conditioned and stored before and after sampling. Sample preparation was performed under a portable laminar flow bench. Both the container and the laboratory were powered by a 10 KVA diesel power generator. In order to avoid contamination, this was installed at 160 m north of the container (Figure 2). Northerly winds are really rare at the site.

[14] The station was operated between 13 January and 13 February 2006 in order to encompass the entire AMMA SOP0/DABEX field campaign.

2.1. Isokinetic Particle Collector (IPC)

[15] Aerosol sampling was performed using two identical inlet systems novelty designed for the AMMA field campaigns. The objectives of this instrumental development were twofold. First, the inlets should be able to serve, on the same air mass, online instruments and filter sampling. Second, distortion in the aerosol size distribution should be minimized. This was true in particular for particles in the coarse fraction, which dominate the mass size distribution of mineral dust aerosols.

[16] The inlet system, called IPC (Isokinetic Particle Collector), is shown in Figure 3. It consists in a sampling head (56 mm diameter), which is nearly isokinetic at the mean wind speed ($\sim$6 m s^{-1}) expected at the site in wintertime. The airflow is kept constant at 50 m^3 h^{-1} by a rotating pump (Minijammer 119379–01, AMETEK Kent USA) controlled with a volume flow controller inserted in the airflow (DMT-586A, System-C-Industrie, Saint Paul Trois Châteaux, France). In order to optimize the collection of larger particles, the sampling head is equipped with a wind vane to make it always face the wind.

[17] The sampling head is followed by a 110-mm divergent where particles are decelerated and transported into a

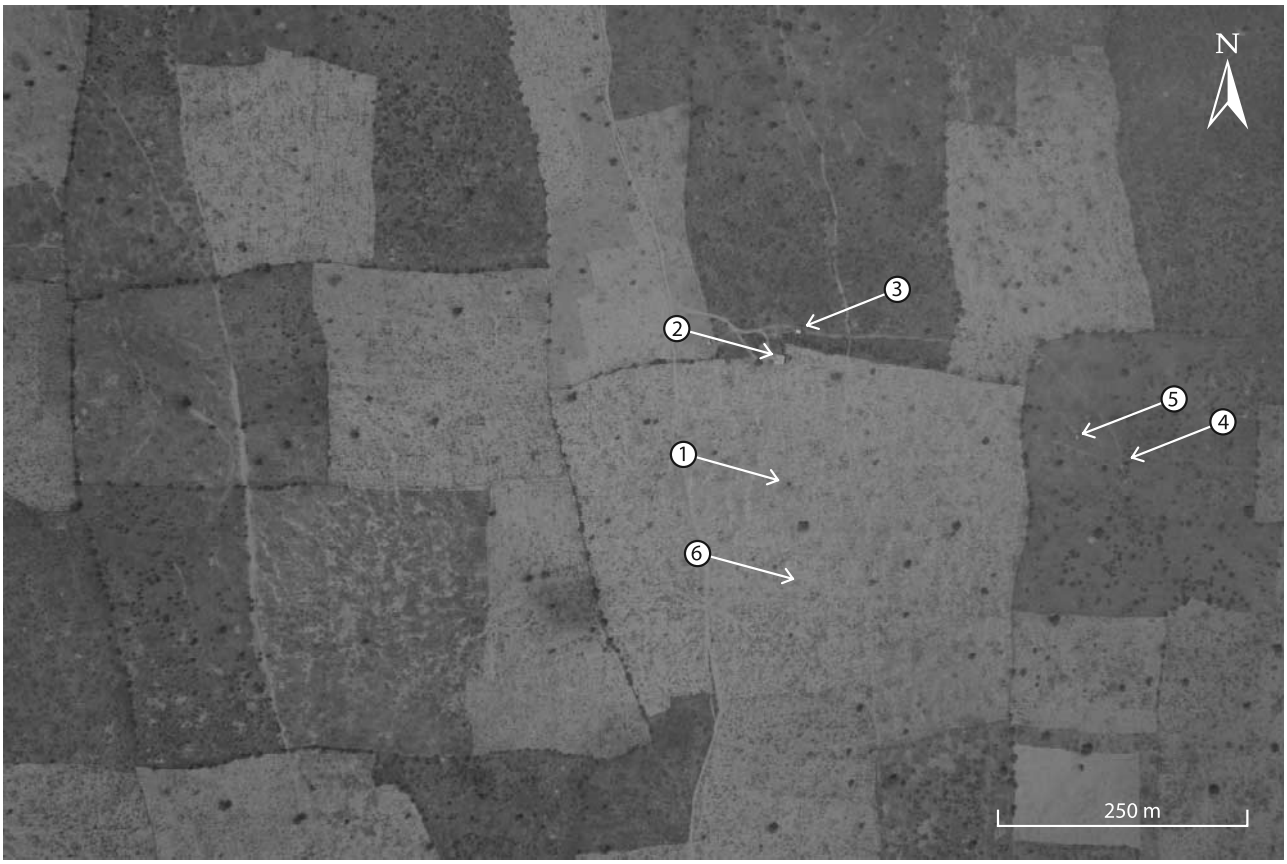

Figure 2. Aerial view of the experimental site on October 2006. Light-colored fields are cropped with pearl millet; dark fields are fallows covered in natural grass and shrubs. Other AMMA experimental devices are also indicated: 1, the buried container and IPC; 2, the laboratory; 3, the power generator; 4, the EOP station; 5, the ARM station, and 6, the heat flux measuring station.

vertical cylindrical chamber (150 mm diameter, 2.7 m high) where 7 sampling lines are inserted. Preliminary calculations suggest that particles of aerodynamic diameter of about 40 μm are transported with 50% efficiency at the entrance of the sampling lines.

[18] The seven sampling lines can be connected to a different online instrument or off-line collector. The diameter of each line is calculated so to match the nominal flow rate needed by instruments. Because of the large number of online instruments and collectors to be installed to document the aerosol physicochemical properties, two IPCs were deployed in parallel (Figure 4). The sampling frequency was fixed at 5 min for the automatic instruments, whereas the exposure times for aerosol collectors such as filters varied according to the atmospheric concentrations. A GRIMM optical particle counter (GRIMM OPC 1.108, GRIMM Aerosol Technik GmbH & Co., Ainring, Germany) was installed behind each IPC in order to check whether the two inlet systems had identical performances in terms of aerosol transmission. The results of this test were very encouraging. For the whole of the campaign, the correlation of particle number measured in parallel on the two IPC was excellent ($R^2 \sim 0.99$). A systematic bias in the slope of the regression line was identified as due to differences in the GRIMM OPCs counting efficiencies and not to in the IPC particle transmission.

[19] In order to avoid perturbation in the airflow and to protect the instruments from the surrounding environment (dust, changes in temperature), an air-conditioned container ($L \times W \times H = 6 \times 2.5 \times 2.5$ m^3) was buried underground and under the IPCs. When doing so, the sampling head of the IPCs was at 2.2 m above ground. The height of the container was sufficient to install all the instruments without bending in the tubing from sampling lines.

2.2. Online In Situ Instrumentation

[20] In this section, we present the characteristics of instruments which are relevant to this paper.

[21] A Tapering Element Oscillating Microbalance (TEOM, model 1400a, Rupprecht and Patashnick Albany, New York USA) was used to measure the total suspended particle (TSP) mass concentration (in μg m^{-3} at standard temperature and pressure (STP; T = 25°C, p = 1013 hPa). The flow rate was 3 L min^{-1} and the averaging time was 5 min. The sample stream is preheated to 50°C before entering the mass transducer so that the measurement is performed always at very low and constant humidity. Moreover, the relative humidity always remained below 45% during the experiment. As a consequence, the TEOM never showed negative values, which indicate generally the occurrence of volatile compounds. The nominal precision of the instrument is ± 5.0 μg m^{-3} for 10 min averaging, which

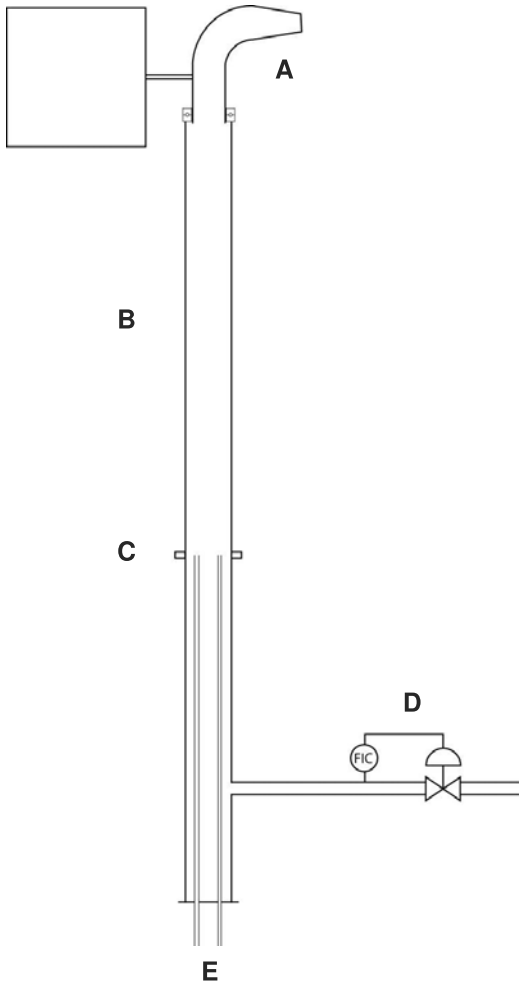

Figure 3. Cross section of the Isokinetic Particles Collector (IPC). Segment A: rotating inlet with wind vane; segment B: mixing chamber; segment C: opening level of the seven sampling lines (only two of them were represented on the scheme); segment D: volume flow controller; and segment E: to the instruments.

is considered as an upper limit for the sampling conditions used during the experiment.

[22] The number size distribution (cm^{-3}) over 15 size classes between 0.3 and 20 μm (optically equivalent particle diameter) was measured by a GRIMM OPC (model 1.108, GRIMM Aerosol Technik GmbH & Co., Ainring, Germany). Aerosols are sampled at a controlled volume flow rate of 1.2 L min^{-1}. Two optical sensors provide near-real-time particle number concentration measurements at a maximum logging rate of 0.17 Hz (or 6 s). Averaging time was 5 min for the experiment.

[23] In order to put into evidence the contribution and properties of coarse particles, and that independently of the total concentration, in the following the normalized mass size distributions $dM/d\log D_p$ calculated from the number size distribution $dN/d\log D_p$ measured by the GRIMM will be presented and discussed. We assumed that particles are spherical, and of homogeneous density of 2.65 g cm^{-3}, typical of the principal minerals (quartz, clays, feldspath, calcite) constituting mineral dust.

[24] Finally, a spectral aethalometer (AE-31, Magee Scientific Company Berkeley, California) was used to determine black carbon (BC) concentrations. The aethalometer is a filter-based instrument measuring light attenuation of aerosol particles deposited through a quartz filter. Flow rate was set to 3 L min^{-1}. The AE-3 series "Spectrum" models of aethalometer use an optical source assembly that incorporates seven different solid-state light sources (370, 450, 520, 590, 660, 880, 940 nm). The content of black carbon (BC) is estimated from the measured optical attenuation at a fixed wavelength λ and the optical absorption cross-section $\sigma(1/\lambda)$. Measurements at 880 nm were used to estimate equivalent BC concentrations. At this wavelength, the contribution of mineral dust to attenuation, although positive, is minimal.

2.3. Filter Collection and Analysis

[25] Samples dedicated to the analysis of the total elemental concentrations were collected on 37-mm polycarbonate Nuclepore membranes of 0.4 μm pore size (Whatman®). The filter lines were equipped with mass flow controllers (BROOKS, model 5850S, Brooks Instrument, Veenendaal, Netherlands) in order to prevent changes in the flow rate due to filter clogging during sampling.

[26] Additional filter collection on 47-mm Nuclepore membranes (0.4-μm pore size) was performed from a PM10 sampling head working at 1 m^3 h^{-1} (Ruprecht and Patashnick, Albany, New York USA), which was installed in parallel of the IPCs on the last part of the campaign (31 January 2006) (Figure 4).

[27] Wavelength dispersive X-ray fluorescence (WD-XRF) analyses have been performed at the LISA in Créteil using a PW-2404 spectrometer by Panalytical. Excitation X rays are produced by a Coolidge tube (I_{max} = 125 mA, V_{max} = 60 kV) with a Rh anode; primary X-ray spectrum can be controlled by inserting filters (Al, at different thickness) between the anode and the sample. Each element was analyzed three times, with specific conditions (voltage, tube filter, collimator, analyzing crystal and detector), lasting 8 to 10 s. Data were collected for nine elements (Na, Mg, Al, Si, P, K, Ca, Ti, Fe) using SuperQ software. The elemental thickness (μg cm^{-2}) was obtained by comparing the filter yields with a sensitivity curve measured in the same geometry on a set of dust certified geo-standards (ANRT GS-N) deposited at different concentrations (<150 μg cm^{-2}) on Nuclepore filters. This range of concentrations corresponds to that expected for African mineral dust in wintertime. The upper limit is fixed so to reduce artifacts related to the auto-absorption of emitted X ray in the sample (matrix effect). Nevertheless this effect still occurred for the lighter elements (Al, Si, P and Mg). A correction factor was estimated by using the slope of the regression line between the ratios of these elements to Fe versus the total estimated mass (sum of analyzed elements per unit surface of the filter). For the AMMA samples, the limit of quantification of the technique ranged between 3×10^{-3} and 13×10^{-3} μg cm^{-2}, depending on element.

2.4. Additional Measurements and Ancillary Data

[28] A saltiphone (Eijkelkamp, Giesbeek, The Netherlands) situated at 5 m from the IPCs allows recording the impacts of sand grain saltating at 9 cm high from the soil

Figure 4. The two IPC samplers standing above the buried container (note the access trap to the container on the right of the samplers and the air conditioning system) and the PM10 Rupprecht and Patashnick Inlet. The field sparsely covered with millet straws is typically grazed by cows during this period of the year.

surface. The occurrence of saltation is due to well-established local aeolian erosion.

[29] A sun/sky photometer of the Aerosol Robotic Network (AERONET) [*Holben et al.*, 2001] was also installed at about 5 km northeast of the Banizoumbou IPCs station. Measured aerosol optical depth at 440 nm and Angström exponent (440–870 nm) will be used in this paper to provide indications of the aerosol seasonal cycle.

[30] PM10 mass concentration (TEOM model 1400a, Rupprecht and Patashnick Albany, New York USA) was also measured at 6.5 m height on a monitoring station set up for the AMMA Enhanced Observation Period (EOP) Wind speed and wind direction (2D sonic anemometer Windsonic, Gill Instrument Ltd.) and air temperature and relative humidity (50Y probe, Campbell Scientific Ltd.) were measured at the same height. The sampling frequency was fixed at 5 min. This station was situated 250 m east of the field (Figure 2).

[31] The origin of air masses corresponding to observed events has been obtained by calculation of 5-day back trajectories. Three-dimensional back trajectories were calculated done with the NOAA HYbrid Single-Particle Lagrangian Integrated Trajectory Model (HYSPLIT). The model uses the $1° \times 1°$ latitude-longitude grid, FNL (acronym for "final") meteorological database [*Draxler and Hess*, 1997]. The 6-hourly FNL archive data is generated by the NCEP's GDAS (National Centers for Environmental Prediction's Global Data Assimilation System) wind field reanalysis. GDAS uses the spectral Medium Range Forecast model (MRF) for the forecast. The FNL database contains basic meteorological field parameters such as the horizontal wind components, temperature, and humidity at 13 vertical levels, from surface level to 20 hPa. Further information on the FNL meteorological database can be found at http://www.arl.noaa.gov/ss/transport/archives.html.

3. Results

3.1. Meteorological Conditions Prevailing During the Measurement Period

[32] Figure 5 locates the SOP0 measurement period within the seasonal cycle of several key meteorological parameters such as the (1) absolute humidity computed from the values of relative humidity and temperature [*Sonntag*, 1990] measured at the EOP station, (2) daily wind direction, and (3) daily maximum wind speed. The dry season, which is characterized by very low absolute humidity values ranging from 2 to 7 g m^{-3}, can be distinguished very clearly on Figure 5a. During this period, the ITCZ is south of the measurement site and the fact that only a few humidity peaks are observed within the surface boundary layer shows that incursions of southern humid air masses to Banizoumbou are rather rare. In the meantime, the prevailing winds blow from the northeast direction (average direction is 45° on Figure 5b), which is typical of the

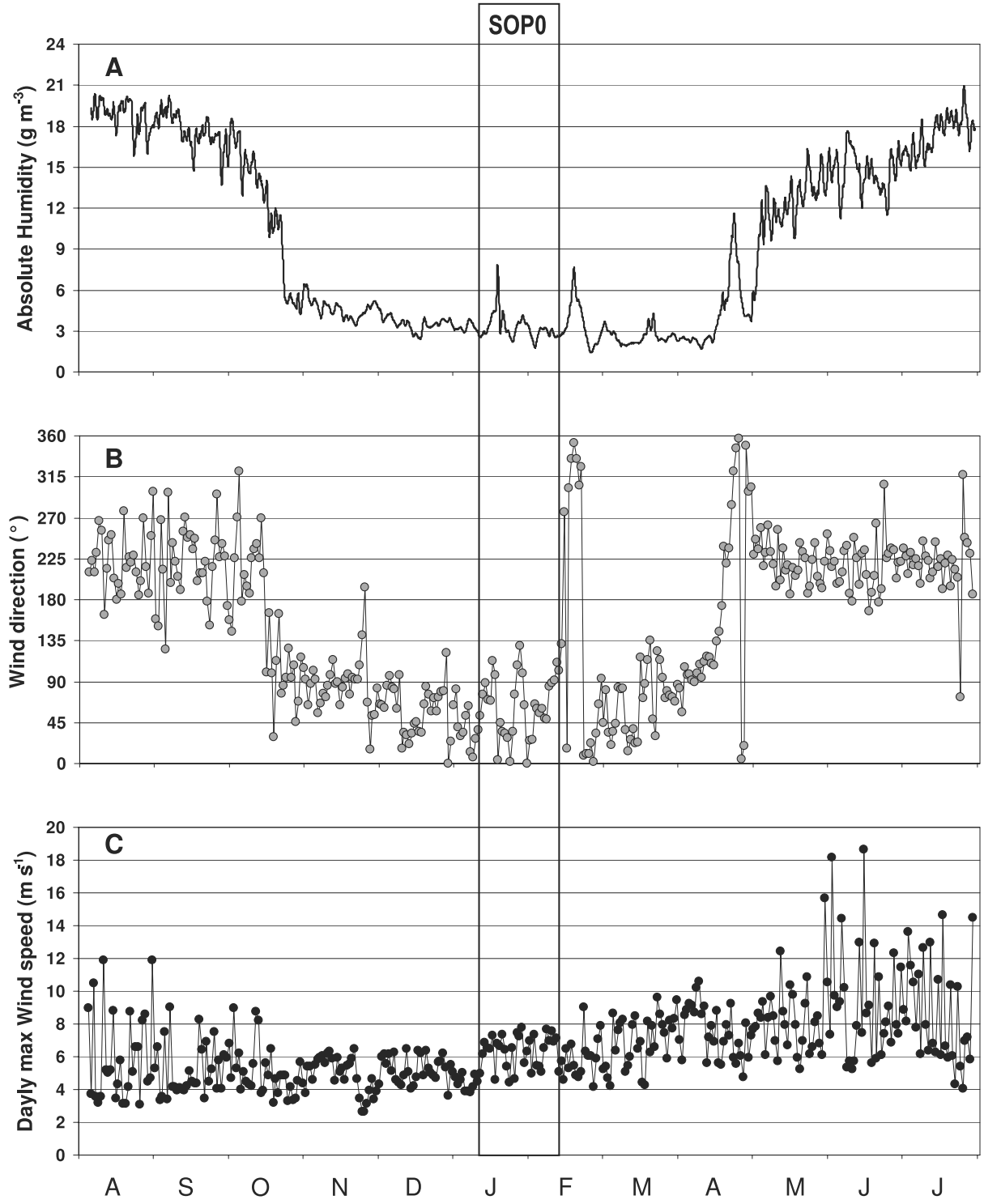

Figure 5. Meteorological conditions during the 2005–2006 dry season. (a) Absolute humidity. (b) Daily mean wind direction. (c) Daily maximum wind velocity. All measurements were made at 6.5 m above ground level at the EOP Station.

Harmattan wind blowing over the Sahel in the dry season. Figure 5 also shows that absolute humidity tends to decrease during the dry season whereas daily maximum wind speed increases. From this point of view, the whole SOP0 measurement period is typical of the mean dry season conditions except for a single event of humid air transport that occurred on 18 January 2006. It can also be mentioned that during SOP0 the daily maximum wind varied significantly between 4 and 8 m s^{-1}.

3.2. Aerosol Loading and Typology During the Measurement Period

[33] The longest survey of aerosol loading available for Banizoumbou is provided by the sunphotometer that was

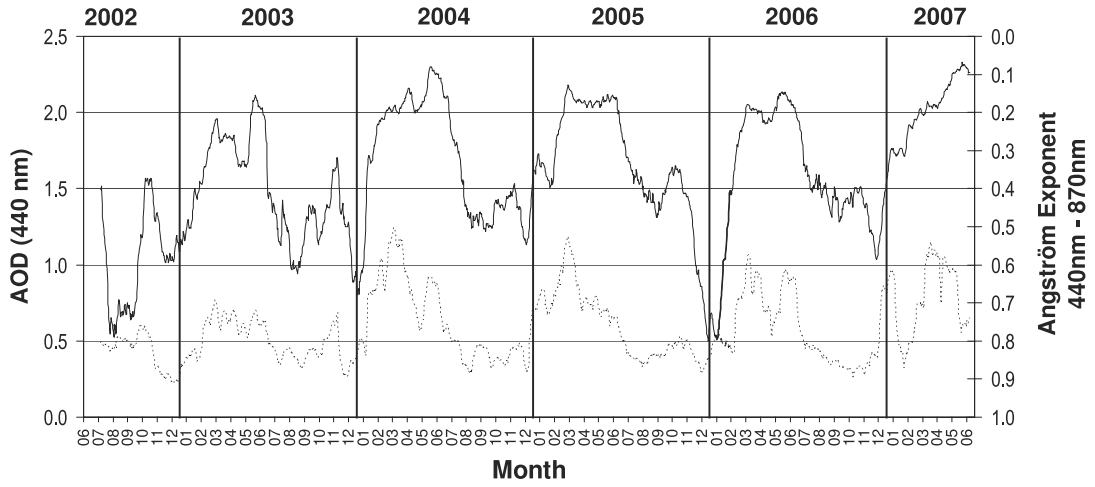

Figure 6. Thirty-day sliding averages of daily aerosol optical depth (AOD) at 440 nm (dotted line) and Angström exponent calculated from AOD at 440 and 870 nm (solid line) derived from the measurements of the AERONET sunphotometer at Banizoumbou. Note that the Angström exponent scale is inverted.

implemented there in 1995 [*Holben et al.*, 2001]. This instrument theoretically provides a continuous record of vertically integrated optical depths and associated retrieved optical properties but owing to some maintenance problems in this remote area there are numerous gaps in level-2 quality assured data set. For this reason, only the more recent, and better quality, measurements performed since 5 July 2002 are used in this work.

[34] The monthly sliding averages of the Aerosol Optical Depth (AOD) at 440 nm ($\tau_{a440\ nm}$) and of Angström's exponent computed between 440 and 870 nm ($\alpha_{440-870}$) for five full years are reported on Figure 6. For a given aerosol type, the AOD is proportional to the atmospheric aerosol load whereas $\alpha_{440-870}$ can be considered as a basic measure of the aerosol size distribution. Indeed, its value is negatively correlated to the proportion of coarse particles in the aerosol. For instance, *Holben et al.* [2001] and *Ogunjobi et al.* [2008] consider that $\alpha_{440-870}$ values less than 0.4 are typical of situations dominated by coarse mineral dust. On the contrary, larger $\alpha_{440-870}$ values denote the presence of submicron aerosol such as those produced by biomass burning or other anthropogenic processes.

[35] Figure 6 shows that over the last 5 years, the aerosol climatology is characterized by a marked seasonal pattern. Between the beginning and the end of February, $\alpha_{440-870}$ decreases dramatically to values lower than 0.3 and increases rapidly again in July. As reported by several authors [*Ben Mohamed et al.*, 1992; *Holben et al.*, 2001; *Ogunjobi et al.*, 2008] the largest AODs are systematically associated with the smallest $\alpha_{440-870}$ but the contrary is not true since $\alpha_{440-870}$ remains low even when the AOD is small. This shows that the coarse mineral dust dominates the overall aerosol during the whole February–July period, that is to say not only during the dry haze events but also in between these large concentration events.

[36] For the rest of the year (from August to February) $\alpha_{440-870}$ is larger and more variable than during the former period. Low $\alpha_{440-870}$ values can be associated with AOD peaks during occasional dry haze events interspersing longer periods which were influenced by finer aerosols. From 2003 to 2006, the largest $\alpha_{440-870}$ have been recorded between December and January. They are usually attributed to biomass burning which is widespread in this period in the Sudanese area, south of the sampling site [*Holben et al.*, 2001; *Ogunjobi et al.*, 2008]. Such huge bush fires do not happen in the Niger where vegetation burning is not authorized by the law. This suggests that the carbonaceous aerosols are mainly transported over the site during these months.

[37] Results obtained between 2003 and 2007 show that the variations of $\alpha_{440-870}$ follow the same pattern as the one already described by *Holben et al.* [2001] from the first 2 years (1995–1997) of measurements of the Banizoumbou sunphotometer. This cycle is also consistent with the observations performed by *Ben Mohamed et al.* [1992] in Tahoua, a small town 1.5° north of Niamey. Conversely, the data they collected in Niamey between February 1986 and June 1987 do not display the same trend. As suggested by the previous authors themselves, this is probably due to the fact that the city pollution may have influenced their results. Noteworthy is the fact that the dust cycle does not coincide with the alternance of the two main Sahelian seasons. Indeed, the influence of mineral dust begins to be clearly dominant only after the middle of the dry season and continues doing so well after the beginning of the rain season.

[38] Though the measurements have been performed for five full years only, an interannual variability can already be noted. For instance, with lower AODs and larger $\alpha_{440-870}$s, the dust period in 2003 is less marked than during the other years. Similarly, the influence of fine aerosols has been particularly pronounced in 2002, and even more so in December 2005 and January 2006.

[39] In summary, with its average $\alpha_{440-870}$ and AOD (0.58 ± 0.25 and 0.47 ± 0.22, respectively) SOP0 is located in a transition zone between the period influenced by carbonaceous aerosols and the one dominated by mineral dust. It also happens to have been performed in the year when the importance of the carbonaceous component in December/January has been the largest of the 5-year reference period.

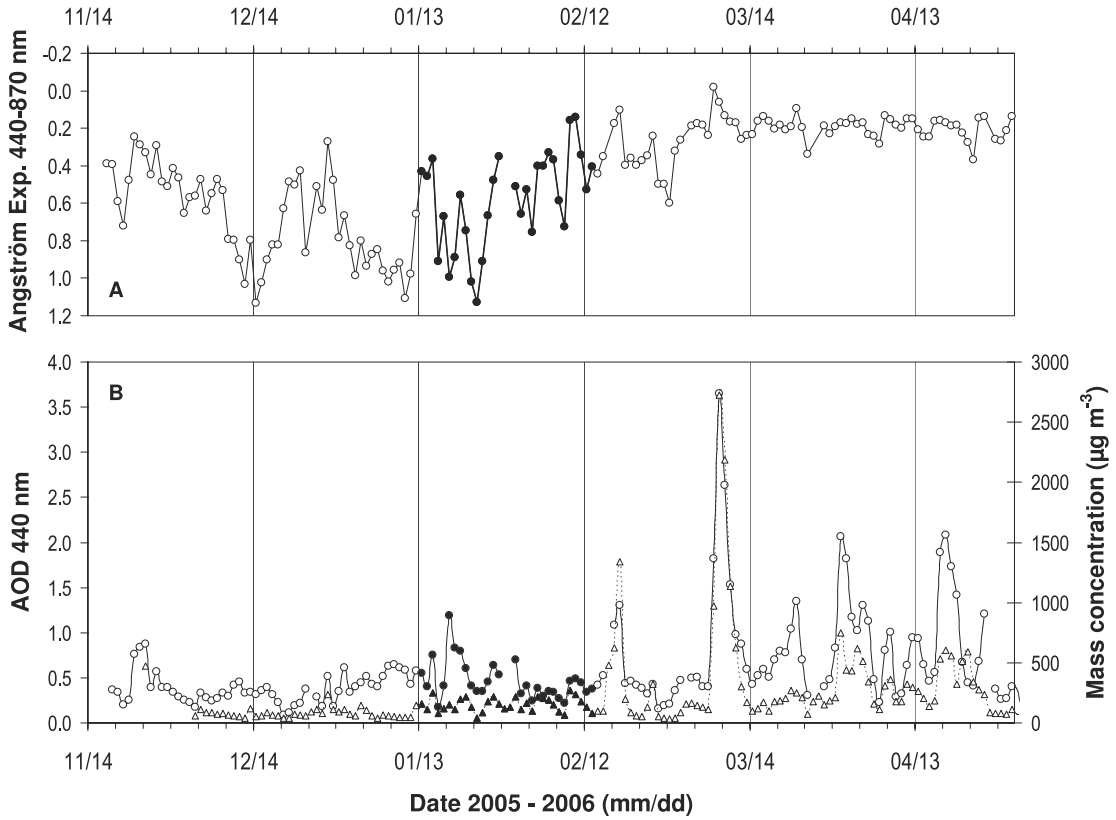

Figure 7. (a) Time series of daily Angström exponent and (b) comparison of daily AODs (circles and solid line) measured at 440 nm by the AERONET sunphotometer with the daily surface level mass concentrations (triangles and dotted line) measured by the TEOM microbalance at the AMMA EOP station. Data collected during the SOP0 measurement period appear in black.

3.3. Aerosols Dynamics During the 2005–2006 Dry Season

[40] The continuous recording of PM10 mass concentration performed at the EOP station since the end of 2005 can be used to assess the characteristics of the SOP0 dust load within the broader frame of the entire dry season. Figure 7b, which compares the daily means of the PM10 to those of the AOD measured at 440 nm by the sunphotometer, reveals that these two quantities are largely independent at the beginning of their common measurement period but tend to covary after mid-January. Note the exception of 18 January which corresponds to an intense biomass burning event which will be discussed later. This link between AOD and surface mass concentration shows that aerosols present in the atmospheric column are also detected at ground level, or in other words that they are not transported in upper air levels only. The fact that the aerosol causing the AOD enhancement are also able to increase the surface mass concentration suggests that they are made of coarse, and hence heavy, particles such as mineral dust rather than of fine carbonaceous particles. This is well confirmed by the low Angström Exponent values (Figure 7a) observed during the second period.

[41] Conversely, the lack of correlation of PM10 and AOD at the beginning of the measurement period (and during 18 January) suggests either that the aerosols are then transported aloft without reaching the ground and/or that they are made of light carbonaceous particles unable to influence significantly the mass concentration measured at the surface. These results are consistent with the observations already discussed above and with the generally higher Angström Exponents confirming the occurrence of small carbonaceous particles. In this temporal frame, SOP0 is located in the period when AOD and PM10 began to covary. In addition, even though the major dust events of February and March 2006 [*Slingo et al.*, 2006] occurred after the end of SOP0, the daily means of the PM10 measured during this period are typical of the second part of the dry season.

3.4. In Situ Measurements

3.4.1. Identification of Intense Episodes

[42] As shown in Figure 8, the time series of the TSP mass and number concentrations (measured by the TEOM and GRIMM OPC, respectively), were highly correlated.

[43] A number of episodes are evident above a relatively constant background of about 100 μg m^{-3} (by mass), corresponding to a particle number concentration of about 30 cm^{-3}. By selecting mass concentration values exceeding 200 μg m^{-3}, three types of episodes could be identified unambiguously: (1) episodes D_i, corresponding to peaks both in mass and number concentrations; (2) episodes L_i, corresponding to peaks in mass concentration only; and (3) episodes B_i, corresponding to peaks more prominent in number than in mass concentration.

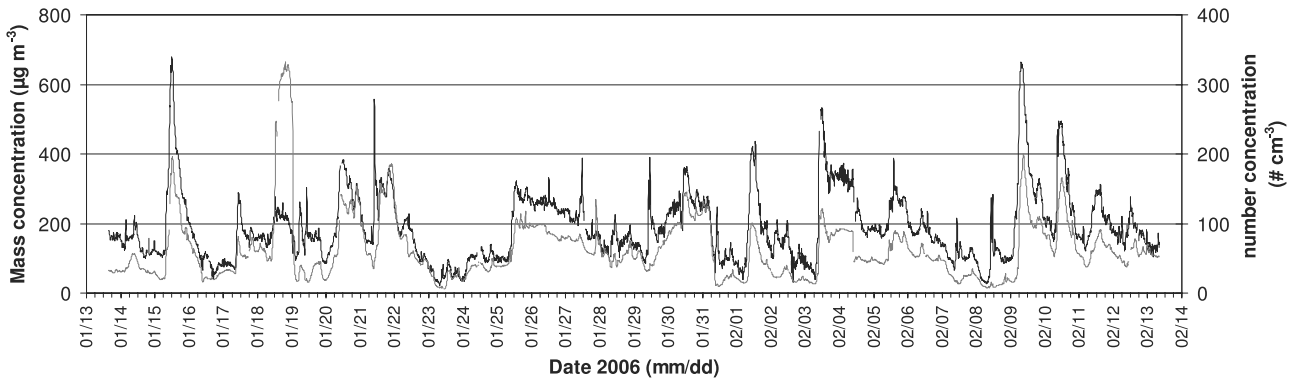

Figure 8. Mass (black line, left axis) and total number (gray line, right axis) concentrations measured downstream of the IPC during the SOP0.

[44] Among episodes meeting at least one of these criteria, we only retained those for which at least one filter sample was available, and for which the XRF analysis was possible. In total, 5 episodes of type L_i, 13 episodes of type D_i and 2 episodes of type B_i were retained (Figure 9). The characteristics of these episodes are shown in Table 1.

[45] On the basis of their composition (see section 3.4.3), episodes of type D_i and L_i are attributed to advection of mineral dust. These two types of episodes are characterized by similar mass concentrations values, but different duration. Type D_i events lasted on average 19 (±13) hours, whereas the duration of episodes of type L_i never exceed 3 hours. Furthermore, these events occurred systematically at the same time of the day (1000 local time), which is not the case for episodes D_i.

[46] No particular conclusion regarding time occurrence can be drawn for the type B_i episodes, which were detected only on two occasions. These events are characterized by an enhancement more important in the number than in the mass concentrations. As discussed in section 3.4.3.3, these episodes could be associated unambiguously to intrusion of biomass burning aerosol-laden air masses from the south.

3.4.2. Dynamics of Local Emission and Advection of Mineral Dust

[47] The role of surface layer dynamics on the occurrence of episodes D_i and L_i is investigated by looking at the surface wind speed (6.5 m above ground). Figure 10 shows the time series of the surface wind speed measured during the experiments. Values corresponding to the episodes are identified.

[48] The temporal behavior of wind speed is characterized by a well marked daily cycle which is typical of the Harmattan period [*Dubief*, 1979]. Wind speeds are low at night, and they increase abruptly in morning, reaching their maximum around 1000 local time, because of the thermal instability induced by solar insulation. Events of type L_i are associated to these thermal winds, occurring when wind speed exceeds 6 m s^{-1} and ending when the wind speed decreases below this threshold. This suggests that episode L_i is due to local emission due to soil erosion in the proximity of the sampling site. It is worth mentioning that, during those episodes, no saltation could be measured at the site. However, the visual observation of creeping sand grains suggests that the wind speed was just reaching the erosion threshold.

[49] Beside the daily cycle, longer-time variability seems to exist. Periods of few days with higher mean wind speed could be identified (19–21 and 27–29 January; 7–12 February) in contrast to few-day periods characterized by low wind speeds (23–24 January; 4–6 February). These two types of period are concurrent with the episodes of type D_i, which occurred even if the wind speed did not reach the

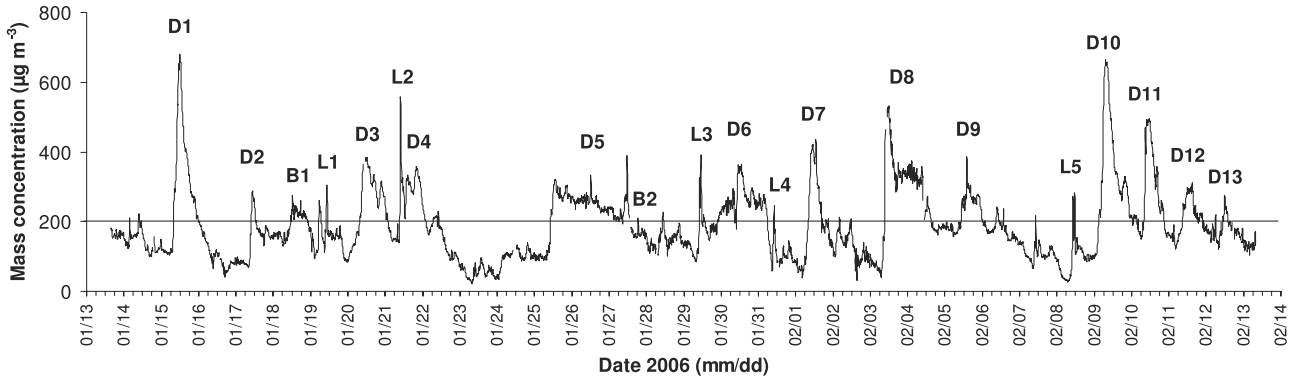

Figure 9. Time series of the mass concentration (μg m^{-3}) during the SOP0 period in Banizoumbou. Peaks corresponding to outbreaks of mineral dust or biomass burning aerosols are indicated. Abbreviations: D, long-range advected dust; L, locally produced dust; B, episodes of transported biomass burning.

Table 1. Characteristics of the 20 Events of Elevated Aerosol Load Observed at Banizoumbou During January–February 2006[a]

Event Identification	Date of Beginning (dd/mm/yyyy local time)	Duration (hours)	Maximum Mass Concentration (μg m^{-3})	Maximum Number Concentration (number per cm^{-3})	Average Particle Mass (10^{-6} μg)	Number of Filters[b]
L1	19/01/2006 1005	0.8	332	23	14.4	1
L2	21/01/2006 0940	2.7	615	71	8.7	1
L3[c]	29/01/2006 0950	2.9	449	45	10.0	1
L4	31/01/2006 0950	0.4	301	16	18.8	1
L5[c]	08/02/2006 1010	0.8	364	17	21.4	1
Average		*1.5*	*412*	*34*	*14.7*	
STD		*1.2*	*126*	*24*	*5.5*	
D1	15/01/2006 0745	16.8	691	202	3.4	2
D2	17/01/2006 0950	3.1	304	84	3.6	1
D3	20/01/2006 0745	18.1	523	155	3.4	1
D4[d]	21/01/2006 0920	16.7	361	186	1.9	1
D5	25/01/2006 1005	50.8	450	157	2.9	7
D6	29/01/2006 2150	31.9	429	148	2.9	6
D7	01/02/2006 0745	9.4	570	101	5.6	3 (3)
D8	03/02/2006 0910	30.1	642	123	5.2	3 (3)
D9	05/02/2006 1020	13.9	504	93	5.4	1 (1)
D10	09/02/2006 0250	24.5	670	202	3.3	3 (3)
D11	10/02/2006 0800	13.0	612	171	3.6	2 (2)
D12	11/02/2006 0840	12.8	356	92	3.9	1 (1)
D13	12/02/2006 1035	3.4	305	66	4.6	1
Average		*18.8*	*494*	*137*	*3.8*	
STD		*13.0*	*138*	*47*	*1.1*	
B1[e]	18/01/2006 1000	15.3	333	348	1.0	2
B2[e]	27/01/2006 2050	4.2	204	142	1.4	1

[a]Denoted by number and/or by mass.
[b]Number in bracket indicates the quantity of PM10 filters available per event (see text).
[c]Not continuous.
[d]Beginning difficult to determine because mixing with local event L2.
[e]Event date and duration determined from number concentration (0.3–0.4 class > 30 particles per cubic centimeter).

threshold value of 6 m s^{-1} (Figure 10). These events generally reach maximum concentration when wind speed is high, i.e., when turbulence is maximum, but they started systematically before wind speed reached its maximum, and may last at nighttime when the wind is almost null (Figure 10). In conclusion, the lack of direct correlation between the surface wind speed and the occurrence of episodes D_i indicates that these are due to synoptic-scale advection of dust from distant sources.

[50] These conclusions are further supported by the lidar observations of the aerosol vertical profile also performed at Banizoumbou during the SOP0 [*Heese and Wiegner*, 2008]. The time series of the vertical profile for the aerosol backscatter coefficient measured on 19 January shows a surface layer existing only between 1015 and 1030 local time, well in agreement with the maximum wind speed and with the occurrence of episode L_1.

[51] Conversely, the time series of the vertical profile for the aerosol backscatter coefficient measured on 15 January shows that the increase of dust concentrations measured at the surface (episode D_1) is due to turbulent mixing at sunrise, when a dust-laden air mass located between 0.5 et 0.9 km above ground at nighttime is mixed with

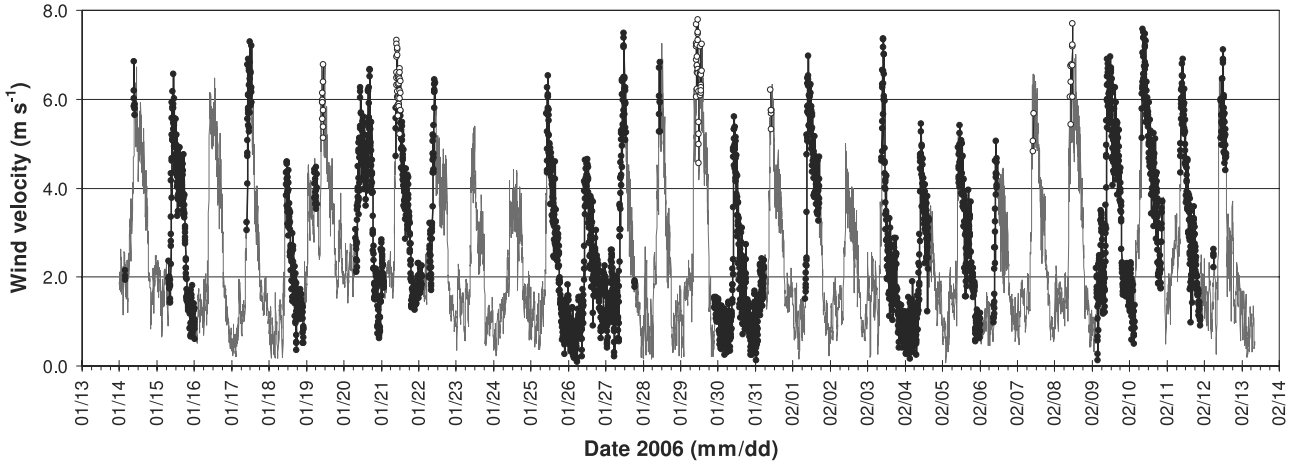

Figure 10. Time series of wind speed during SOP0. Open circles correspond to L events and solid circles correspond to either D or B events. See text for the definition of these types of events.

Table 2. Mean Elementary Composition for the Whole Set of Bulk TSP Filters Sampled at Banizoumbou During January–February 2006

	Elements							
	Mg	Al	Si	P	K	Ca	Ti	Fe
Mean composition (%)	2.6	20.5	54.1	0.24	3.7	6.5	1.5	10.9
STD (%)	0.9	1.6	2.0	0.03	0.8	1.5	0.3	0.7
Coefficient of variation (%)	15.1	7.7	3.7	13.3	20.8	23.0	17.6	6.5

the stable dust free surface layer of the night. Then, the surface dust layer persisted through the day.

3.4.3. Elemental Signature of the Individual Episodes

[52] The aerosol total elemental composition has been determined from the 76 filters collected during the field campaign. The mean percent composition (±standard deviation) estimated from the measured elements (Mg, Al, Si, P, K, Ca, Ti, Fe) is shown in Table 2.

[53] Al and Si represent ~75% of the analyzed elemental mass, indicating that the variability of measured mass concentrations is related to the occurrence of mineral dust. The contribution of BC from biomass burning (not included in Table 2) is minor, accounting at the maximum for 5% of the total mass measured by the TEOM for an episode of exceptionally high BC concentrations (see below).

[54] A statistical treatment of the elemental fingerprinting of the aerosol composition, and its variability, has been obtained by Principal Component Analysis (PCA) available within the Statistica© software package. The PCA data treatment consists in identifying common factors (or axis) based on the covariance of the time series of elemental concentrations. These factors can be associated with mineralogical families, which might, or might not, represent a source. This treatment was applied to the entire filter database, including the PM_{10} filters which had started been collected from 31 January onward.

[55] Three factors (axis) were identified, allowed representing the 90% of the total variability of elemental concentrations during the field campaign. Each of them accounted for 46, 26 and 17% of the variability, respectively. The first factor (F_1) is controlled by Ti, Fe, and Al, and by Ca and Mg in opposition (Figure 11a). Correlation coefficients of these elements with F_1 are respectively: 0.87, 0.83, 0.79, −0.83 and −0.81. The second factor (F_2) is controlled by Si (0.96) (Figure 11a), and the third (F_3) by K (−0.85) and P (−0.71) (Figure 13a in section 3.4.3.3). The next step is looking at how the measured concentrations are represented by these factors. For sake of clarity, we will limit the discussion to the 20 episodes identified. This represents 40 TSP filters, and 13 PM_{10} filters.

3.4.3.1. Episodes Type D_i: Synoptic-Scale Advection of Dust From Distant Sources

[56] Thirty-two TSP and 13 PM_{10} filters were collected during type D_i episodes. These are represented by factors F_1 and F_2. Filters corresponding to a single episode grouped in clusters and showed little variability, whereas different episodes well separated along the axis (Figure 11b). This suggests that, while the elemental composition does not change during an episode, different episodes might have different composition. This can be explained by looking at 5-day back trajectories calculated in correspondence of each episode (Figure 12). Episodes with different composition (such as D_1, D_3, D_7) correspond to transport from different regions, whereas episodes for which the composition is similar, correspond to air masses of similar origin (such as D_3 and D_5). Differences in composition therefore represent differences in source region of emission.

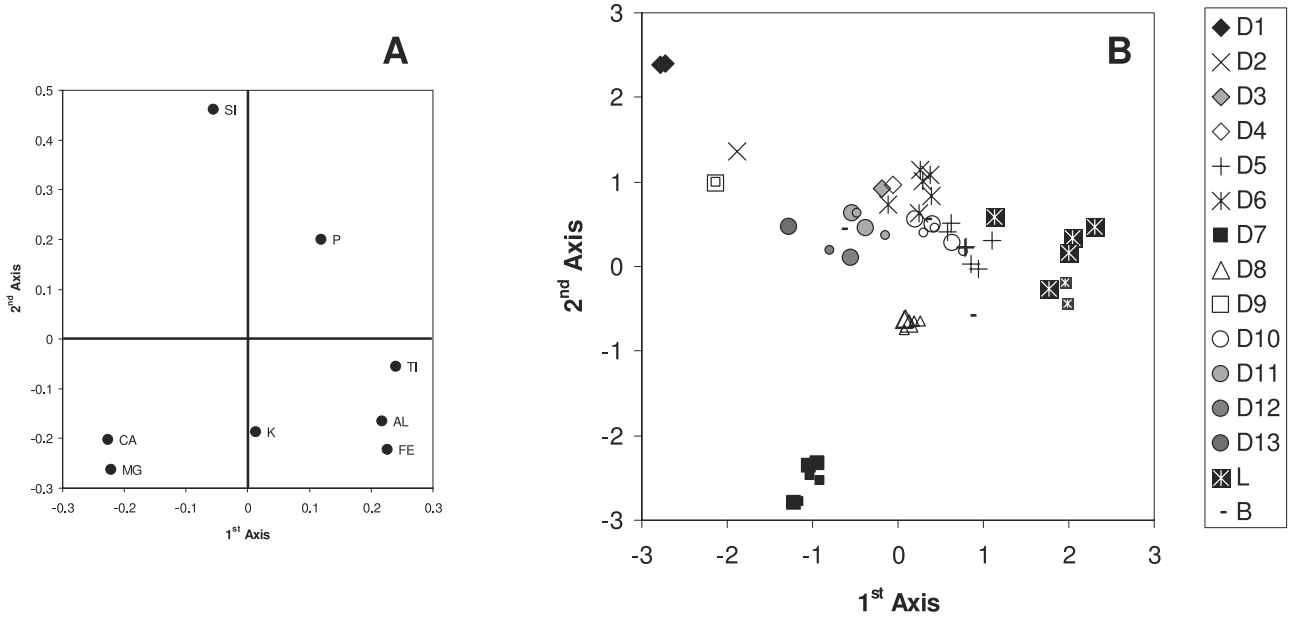

Figure 11. Results of principal component analysis (PCA) performed on the time series of TSP bulk elemental concentrations for Banizoumbou during the SOP0. (a) Element weight for first and second axis. (b) The 20 identified events plotted according to first and second axis identified by PCA. Small symbols correspond to PM10 samples. See text for details.

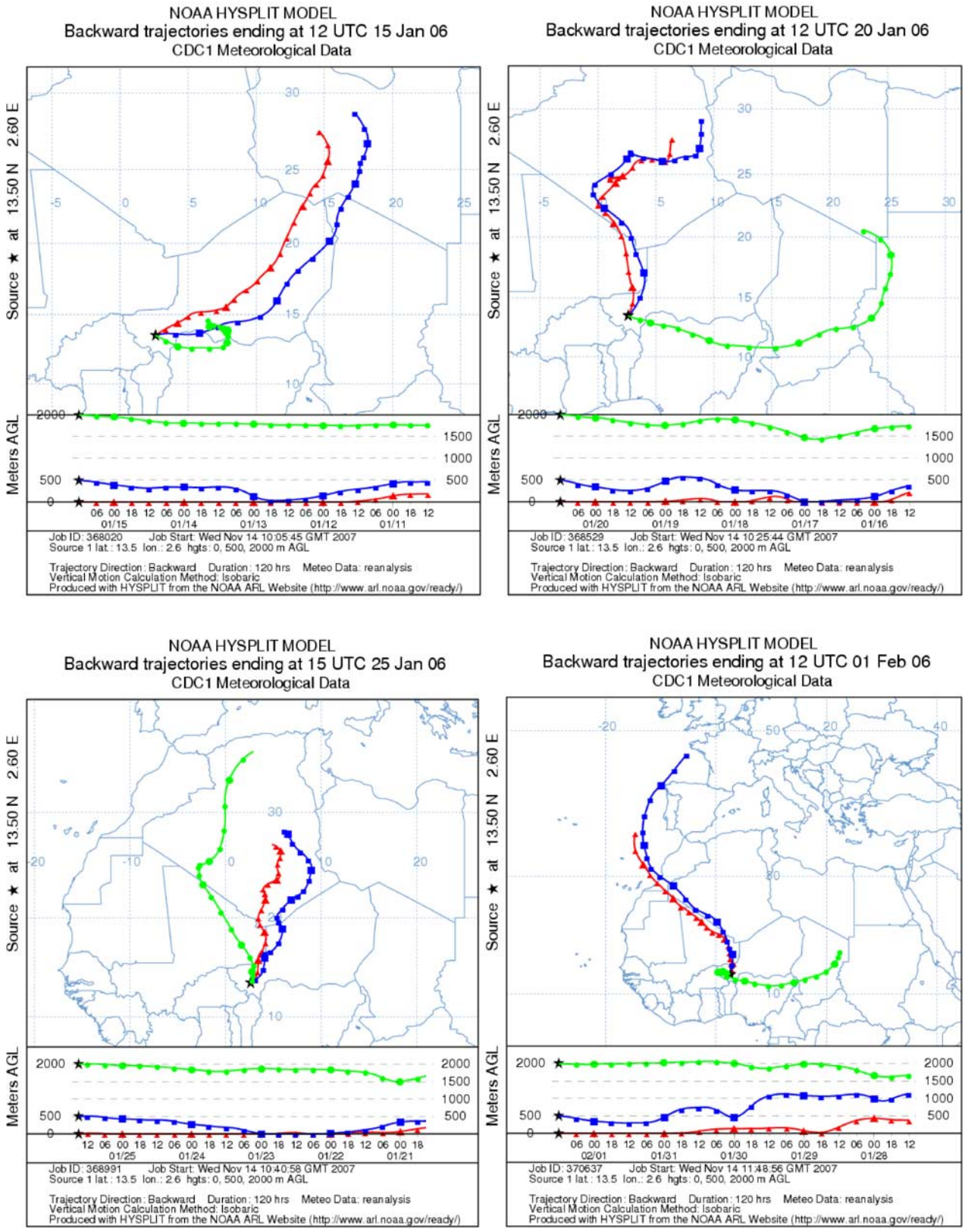

Figure 12. Five-day air mass back trajectories for the D1, D3, D5, and D7 dust advection cases. Calculations are performed at 0, 500, and 2000 m above ground level (agl).

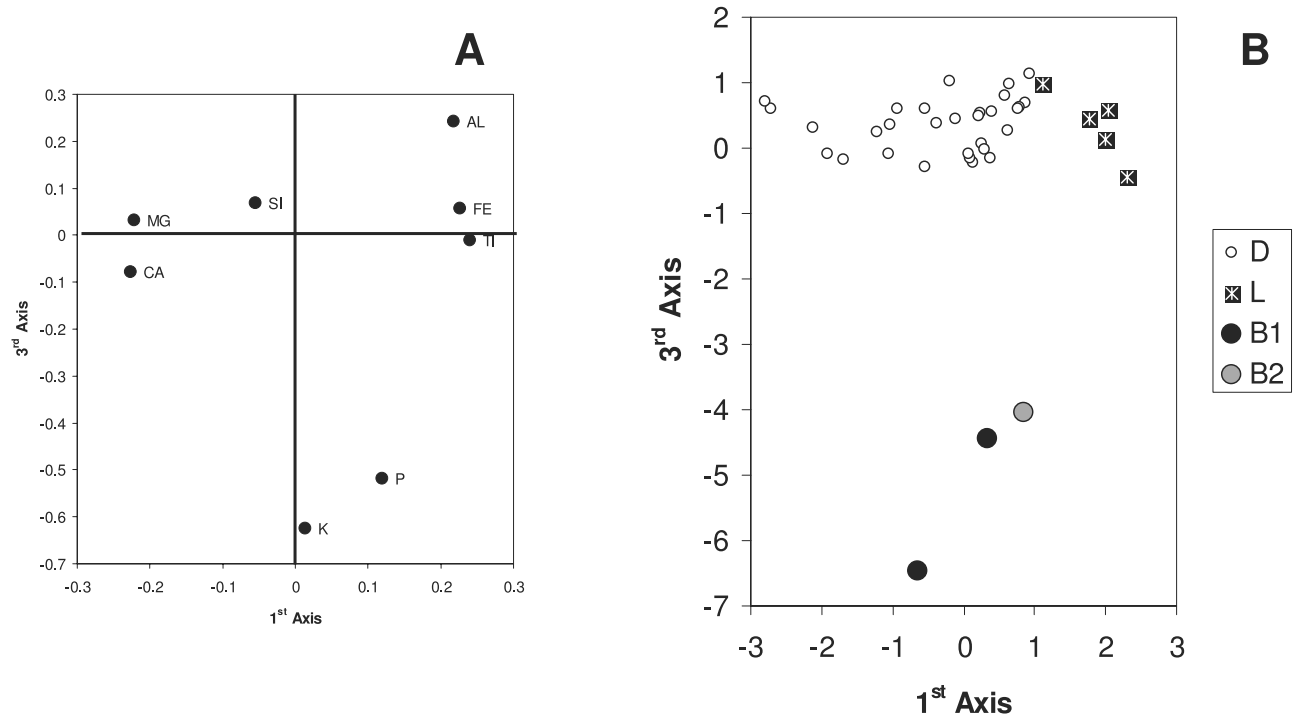

Figure 13. Results of principal component analysis (PCA) performed on the time series of TSP bulk elemental concentrations for Banizoumbou during the SOP0. (a) Element weight for first and third axis. (b) The 20 identified events plotted according to first and third axis identified by PCA. The two biomass burning events are clearly isolated.

3.4.3.2. Episodes Type L_i Local Emission

[57] Five TSP filters were collected during type L_i episodes. These converge into a close cluster along the F_1-F_2 axis (Figure 11b). F_1 is the dominant factor; that is, they are enriched in Fe, Ti and Al, and conversely poor in Ca and Mg. This is in good agreement with previous measurement performed during wind erosion episodes in the area [*Rajot and Valentin*, 2001], thus with their supposed local origin. One only episode (L_2) presented a moderate Fe-Al signature, and a composition closer to that of the type D_i episodes of advection. As a matter of fact, episode L_2 just preceded that of episode D_4. Its composition likely represents a mixture between those of locally emitted and advected dust. This kind of mixing is difficult to detect, as in wintertime local emission episodes are of very low intensity and duration. However, the threshold wind speed of 6 m s^{-1} above which local erosion is triggered has been reached several times during advection cases. In this case, it can be expected that at least some amount of locally produced dust should be mixed with the transported one. In order to estimate in what proportion local dust is present in the mixing, the following assumptions have been made: (1) over the short duration of local events, the concentration in advected dust varies linearly; and (2) local erosion occurs at wind speeds larger than 6 m s^{-1}. Under these assumptions, the part (L_{Ti}) of the concentration C_i measured by the TEOM during a mixed local/transport event that is really due to local emission can be expressed as

$$L_{Ti} = C_i - \frac{C_a + C_b}{2}, \quad (1)$$

where C_b and C_a are the concentrations due to transported dust only and measured immediately after and before the local erosion period.

[58] By doing so, the contribution of local erosion to the overall dust concentration measured during SOP0 is found to be on the order of 1.5%.

[59] Finally, it must be noted that the determination of the elemental signature of local erosion episodes have been possible only when sampling was of very short duration, performed very close to dust concentration peaks and in absence of advection.

3.4.3.3. Episodes Type B_i: Biomass Burning Emission Aerosols

[60] Three TSP filters were collected during type B_i episodes, which are attributed to advection of biomass burning aerosols. As a matter of fact, episodes B_i are characterized by enrichment in elemental potassium (represented by factor F_3; Figure 13) good tracer for aged biomass burning [*Gaudichet et al.*, 1995], and are associated to air mass originating from South of the Sahel Zone (Figure 14), where fire activity is important at this time of the year. These episodes of long-range transport are clearly evident when looking at the time series of the attenuation measured at 880 nm by the aethalometer (Figure 15). Attenuation varied between 0.1 and 4.5, the highest value being measured during episode B_1. Attenuation may be due to dust or black carbon. Dust events such as D1 (15 January) or D10 (9 February) are easily recognizable. Beside those episodes, attenuation tends to be higher at nighttime when the boundary layer is stable. Local sources of BC are domestic wood burning, generally done twice a day in the morning

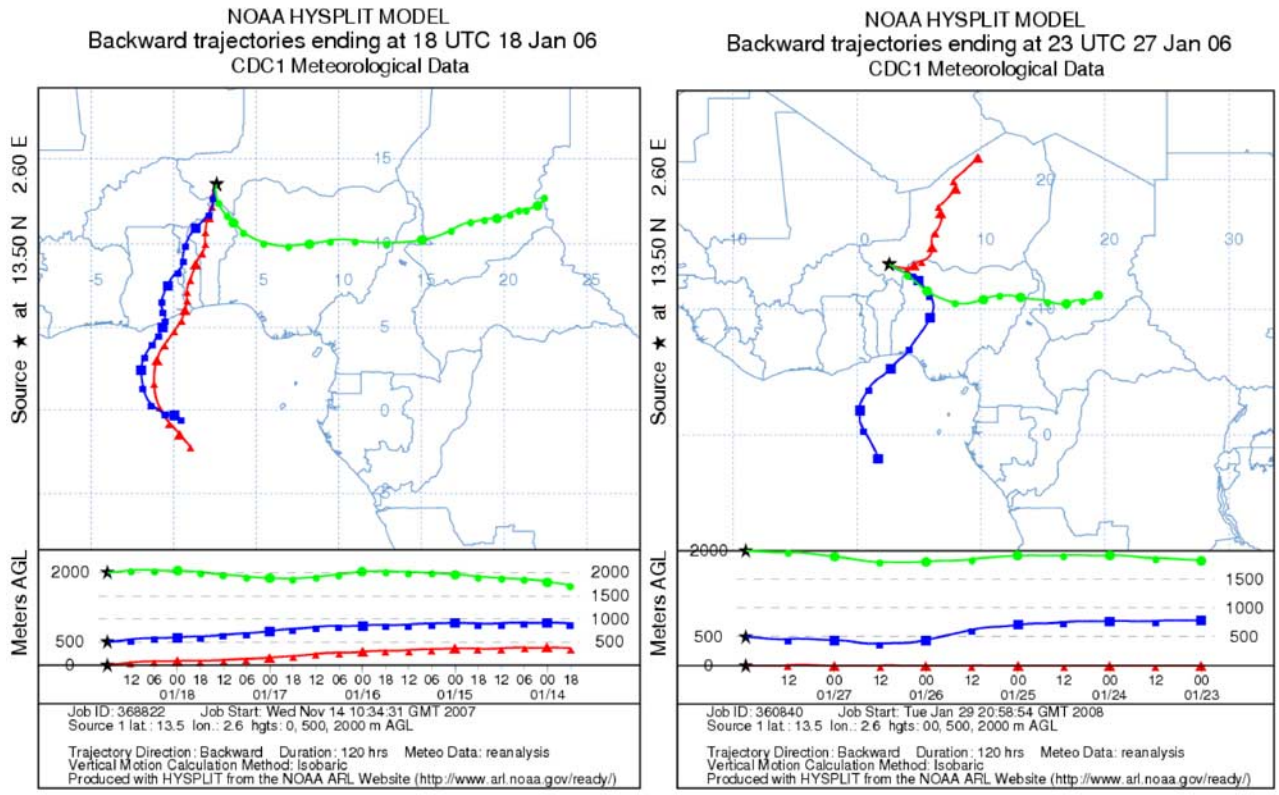

Figure 14. Five-day air mass back trajectories for the two biomass burning events B1 and B2. Calculations are performed at 0, 500, and 2000 m agl.

and in the evening, and fires for disposal of shrubs which have been cleared from the fallows assigned to millet cultivation during the next rainy season. Owing to legal regulation, these last fires are scarce and only occurred at nights when wind speed is low enough to avoid uncontrolled extension of the fire. Conversely, no contribution from road traffic is expected as the closer road is at 12 km from the sampling site.

3.4.4. Aerosol Size Distribution

[61] The mass fraction of particles coarser than 7.5 μm, a limit that has been chosen because it separates two different particle populations (see below), can be derived simply from the aerosol size distribution measurements performed with the GRIMM optical counter. The results of this computation (Figure 16) show that this proportion fluctuates between 10% and a little more than 60% during the

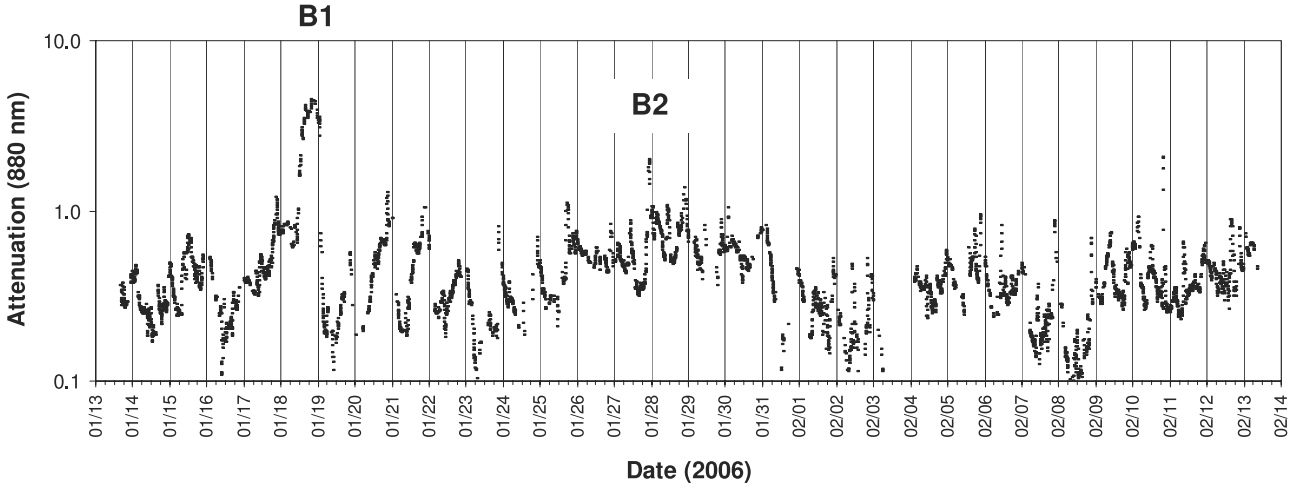

Figure 15. Aerosol attenuation measured at 880 nm by the seven-wavelength aethalomètre. The two biomass burning events B1 and B2 are indicated.

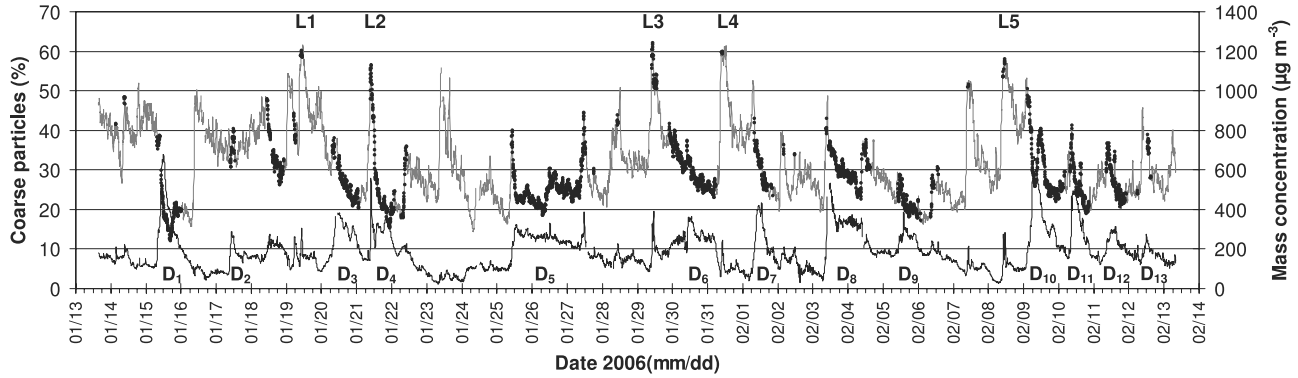

Figure 16. Mass fraction of coarse (optical diameter > 7.5 μm) particles during the SOP0 campaign. Periods when mass concentration is >200 μg m^{-3} are outlined (black dots). The time series of mass concentration (thin black line) is also reported in order to locate the D_i episodes maxima.

measurement campaign. The largest values are clearly those associated with local erosion events. During these L-type events the proportion is always larger than 50%. Conversely, the lowest values are obtained during the D-type events. Noteworthy is the fact that during these events the size distribution is not stable. Indeed, a decrease with time of the importance of the coarse particles is generally observed, for events D3, D4, D6, D7, D8, D11, and D12, for instance. However, coarse particle peaks can also be observed occasionally, as during D1, D5, and D10. These size distribution changes observed during advection events of D type could be due to the mixing of coarse particles produced locally with finer aerosols that have undergone long-range transport, as for already described L2 and D4 events mixing. For the other events, the decrease in the proportion of coarse particles is less clear. It could either be due to the increasing proportion of fine-transported particles in a relatively coarse background aerosol, or to the fact that the front of the transported plume is richer in coarse particles than the tail.

[62] The typical size distributions corresponding to each type of events are represented on Figure 17. In this representation, the early stages of the type D events have been distinguished from the late ones. Practically, each reported size distribution is an average of the measurements performed over periods when the proportion of coarse particles remained stable (±5%). The duration of these periods varies between 35 min and 5 h. For the L-type events, computations have been made over the whole duration of the event. B1 and B2 are also represented but the beginning and the end of the event have been separated for B1 only.

[63] The most striking feature of Figure 17 is the commonality in size distribution of events belonging to a given type. Contrary to what was observed with elemental composition that could differ from one D event to the other, no distinction can be made between these events on the ground of their size distribution. Two particles populations can be distinguished on the size distribution: one coarse mode (mode 1) located in the 7.5- to 10-μm size class (geometric mean = 8.66 μm) and a finer one (mode 2) in the 4- to 5-μm

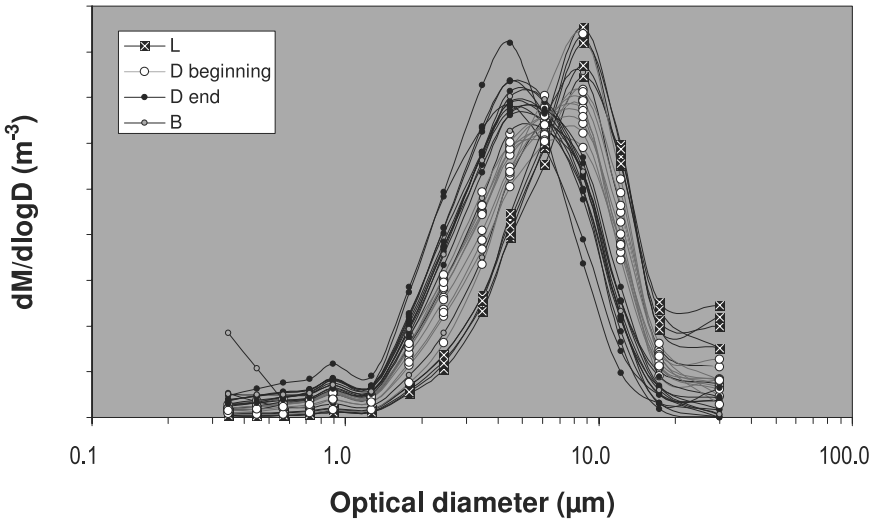

Figure 17. Normalized mass size distributions for the three different types of events. For the type D events, the two extremes of the size distribution are represented. The first (second) corresponds to the beginning (end) of the event; in this case the mass fraction of the coarse particles is the largest (lowest, respectively).

size class (geometric mean = 4.47 μm). During L events, mode 1 is clearly dominant whereas D events are made of a mixture in varying proportions of modes 1 and 2. More precisely, the importance of mode 2 in this mixture increases with time during a given event.

[64] A close examination of the mass of particles present in the largest size class of the GRIMM counter suggests that a third particle population (mode 0) too coarse to be characterized with the optical counter could also be present in the aerosol. It seems that the amplitude of this mode could be decreasing progressively when one goes from L to early D, and finally to late D events. On the other side of the size spectrum, the contrary is observed for a submicron population whose mode is located approximately between 0.8 and 1 μm.

[65] The only difference between the size distribution of the B-type events and those of the L and D type lies in the presence of a submicron particle mode below 0.5–0.65 μm diameter. This size has already been recognized as an upper limit for the size of BC particles [e.g., *Clarke et al.*, 2004]. It is also probably in this very fine size range that must be located the bulk of the BC particles detected by the aethalometer outside the B events. Therefore, the rest of the size distribution must be controlled by mineral dust particles. With mode 1 initially dominating and the mode 2 progressively taking over, the B1 event is similar to events of the D type. As for B2, it is dominated by mode 2.

[66] After 31 January, air suspended particles have been collected in parallel on two identical filters, the only difference being in the size cutoff because one of the filters was connected to the IPC and the other to a PM10 sampling head. Elemental analyses performed on the samples confirm by an absolutely independent method the mass size distribution variations retrieved from the optical counter measurements. In particular, the mass fraction of particles larger than 10 μm varies from 8 to a little more than 50% during the whole duration of the common measurement period (not shown). The largest proportion of particles coarser than 10 μm (51%) is obtained during the L5 local event. Large variations are also observed during individual D-type events (e.g., decreases from 42 to 29% and from 28 to 16% during D8 and D10, respectively). These variations are in the same order of magnitude than those deduced from the optical counter measurement, which suggests that the mass of the coarse mode not seen by the GRIMM (mode 0) is significantly less than the cumulated masses of modes 1 and 2 defined above.

[67] The results of elemental analysis performed simultaneously on the PM10 filters and on the TSP ones are reported on Figure 11b. They coincide almost exactly in their projection on axes 1 and 2, which shows that their composition is identical in particular during D-type events. In turn, this last result suggests that modes 1 and 2 should not be significantly different regarding their mineralogical composition.

4. Discussion and Conclusions

[68] The AMMA supersite of Banizoumbou is a remote site located in the middle of the cultivated Sahel, and in the vicinity of some major mineral dust source areas (the northeast desert in Niger and the Bodélé depression in Chad).

[69] In addition to long-term measurements, which have been performed since the early nineties [*Holben et al.*, 2001, *Ogunjobi et al.*, 2008], a sophisticated multi-instrument platform was deployed at the site during the special observation periods of AMMA. The double aim of this experimental setup was to document the atmospheric load in mineral dust produced by wind erosion and carbonaceous aerosols produced by biomass burning, and, at the same time, their compositional and physical properties.

[70] This paper presents time series of meteorological parameters, aerosol concentrations, and aerosol composition in order to illustrate the representativeness of the SOP0 period within the annual cycles of these characteristics. The occurrence of specific episodes of intrusion of advected and locally emitted mineral dust, as well as of biomass burning aerosols, is also highlighted and characterized in terms of their origin, aerosol composition and size distribution.

[71] The major conclusions of this work can be summarized as follows.

4.1. Seasonal Cycle and Interannual Variability

[72] In accordance with previous observations by *Holben et al.* [2001], the column aerosol loading and type are characterized by a seasonal cycle. A first period extending from July to January is characterized by relatively low aerosol concentrations associated with high Angström's exponent values, indicating that the contribution of fine particles, which are probably of biomass burning origin, to the overall aerosol is significant.

[73] During the rest of the year, mineral dust dominates the aerosol load of the atmosphere. Average concentrations are also globally higher and intense episodes more frequent. Remarkably, this aerosol seasonal cycle is not in phase with the meteorological seasonality. Indeed, dust systematic prevalence only starts in the middle of the dry season and lasts well after the beginning of the wet season.

[74] Regarding interannual variability, the 2006 SOP0 period compares well to the four previously documented dry seasons. Indeed, even though it is found that the frequency and contribution of biomass burning episodes to the aerosol optical depth is larger than during the previous years this enhancement remains within the limits of the expected interannual variability.

4.2. Episode Measured at the Surface Level: Height of Transport

[75] Our measurements show that both mineral dust and biomass burning aerosols episodically came close to the surface. The only two episodes of biomass burning that were detected in Banizoumbou lasted for less than 3% of the entire measurement period, and were associated with air masses originating from the south of the Sahel zone. Lidar and aircraft measurements show that layers of biomass burning were more frequently encountered in the free troposphere [*Heese and Wiegner*, 2008; *Johnson et al.*, 2008]. Although longer time series would be needed to confirm this, the fact that biomass burning episodes extended down to ground level is probably more an exception than the rule. This is illustrated by the 18 January 2006 episode, which corresponded to a particular case of recirculation at regional scale of a moist air mass originating from southern Sahel. Such an increase of air moisture at the surface is

exceptional when one looks to the humidity time series of 2005–2006 dry season (Figure 5).

[76] In addition to those produced by large-scale vegetation burning taking place in the south, absorbing aerosols can be released by much smaller local fires used for cooking or land clearing. These carbonaceous particles dominate the aerosol number size distribution below 0.4 μm. Their effect on the aerosol optical properties in the surface layer might not be negligible, and needs being estimated.

[77] Conversely, intense episodes of mineral dust represent 35% of the duration of the whole sampling period. The majority of these episodes were from distant sources. The good correlation between the concentrations measured at the surface and the vertically integrated aerosol optical depth suggests that most of the time dust is transported close to the surface, at least during daytime [*Ben Mohamed and Frangi*, 1986]. Indeed, lidar [*Heese and Wiegner*, 2008] as well as other surface measurements confirm the major part played by dynamics in the formation of concentration peaks recorded at ground level. Those maxima are usually observed around the middle of the day at a time when thermal instability favors vertical development of the planetary boundary layer (PBL) that is thus able to reach the height of the transport layer. Those particles are then homogenized in the mixing layer and transported downward to ground level. Noteworthy is the fact that this process coincides in time with the occurrence of maximal wind speeds at the surface, which can themselves result in local wind erosion provided they become larger than the erosion threshold. Such short duration events have been observed on five occasions when the wind speed recorded at an elevation of 6.5 m above ground and averaged over 5 min became larger than 6 m s^{-1}. Our estimations show that, owing to these events, the contribution of local emissions to the overall mineral dust concentrations recorded during the whole field campaign does not exceed 1.5%. Note that this contribution is expected to increase for at least two reasons during the dry season: (1) the surface wind speed tends to increase with time (Figure 5) and (2) the surface aerodynamic roughness that controls the emission threshold [*Marticorena and Bergametti*, 1995] decreases [*Bielders et al.*, 2004].

[78] A similar diurnal cycle in wind intensity, with the appearance of a nighttime low-level jet and a daytime maximum surface wind when momentum is mixed downward in turbulence, associated to enhanced dust emissions, is described by *Washington et al.* [2006] for the Bodélé depression. *Mbourou et al.* [1997] already observed such a dust diurnal cycle at the Sahelian scale during the dry season. This dynamics linked to low-level jet seems widespread in the Sahel [*Lothom et al.*, 2008]. Depending on surface features and dust load, this low-level jet and turbulence could induce dust emission, entrainment of dust in the PBL or a combination of these two phenomena as it was observed at Banizoumbou.

4.3. Size Distribution

[79] During the measurement campaign, the aerosols volume size distributions are controlled by the mineral dust component. Biomass burning particles are found in the size range below 0.65 μm, this upper limit being measurable only during the two episodes of advection of distant biomass burning. All the measured size distributions can be considered as a mixture of four particle populations. The finest, centered on a diameter slightly smaller than 1 μm, is in part influenced by carbonaceous particles. On the opposite side of the size distribution, the largest population whose mode is probably larger than 30 μm cannot be fully detected with the optical counter. The two intermediate populations are centered on 4.5 and 9 μm, respectively. The modes of the three finest populations are systematically smaller than those (1.6, 6.7 and 14.2 μm), obtained by *Alfaro et al.* [1998]. A possible cause for discrepancy might be the fact that our values have been derived from measurements performed with an OPC calibrated with latex spheres that do not have the same refractive index than mineral particles.

[80] As compared to episodes of long-range transport, local erosion events are characterized by the dominance of the two coarsest particle modes. The very little contribution of the finest modes is quite consistent with the sandblasting theory proposed by *Alfaro et al.* [1998] and *Alfaro and Gomes* [2001]. Indeed, local erosion is due to local winds that are just above the erosion threshold and not strong enough to free the smallest particle populations that are also the hardest to release. Note that it can be expected that this production will become possible only later in the dry season when wind speed become larger than during SOP0 (see above).

[81] All the long-range transport events have similar size distributions dominated by the 4.5 and 9 μm modes. Typically, the 9-μm mode always dominates at the beginning of the event but the importance of the finer mode progressively increases until it dominates toward the end. These size distributions are within the very wide range of size distributions reported by *Goudie and Middleton* [2001].

4.4. Regional Variability of the Mineral Dust Elemental Composition

[82] The statistical analysis of the covariance of the time series of elemental concentrations obtained by filter sampling allows discriminating different types of episodes (advected dust, locally emitted dust, and biomass burning). The episodes of locally emitted dust are enriched in Al, Ti and Fe, and poor in Ca and Mg, which is typical for the region.

[83] The episodes of advection can be classified according to the origin of air masses traced by back-trajectory analysis. Remarkably, the largest differences in composition are obtained for air masses which originated from opposite sectors (northeast and northwest for the episodes of 15 January and 1 February, respectively). These differences in elemental composition also correspond to differences in the mineralogical composition [*Formenti et al.*, 2008]. The next step will consist in establishing whether these compositional differences are reflected in the optical and radiative properties.

[84] **Acknowledgments.** On the basis of a French initiative, AMMA was built by an international scientific group and is currently funded by a large number of agencies, especially from France, UK, United States, and Africa. It has been the beneficiary of a major financial contribution from the European Community's Sixth Framework Research Programme. The authors gratefully acknowledge the NOAA Air Resources Laboratory (ARL) for the provision of the HYSPLIT transport and dispersion model and/or READY website (http://www.arl.noaa.gov/ready.html) used in this publication. The paper is dedicated to the memory of our friend F. Lavenu

who chose and settled the Banizoumbou AERONET site more than 10 years ago. The authors thank the AERONET project, Adamou Ousmane Manga, and Didier Tanré for maintaining the site.

References

Alfaro, S. C., and L. Gomes (2001), Modeling mineral aerosol production by wind erosion: Emission intensities and aerosol distributions in source areas, *J. Geophys. Res.*, *106*(D16), 18,075–18,084, doi:10.1029/2000JD900339.

Alfaro, S. C., A. Gaudichet, L. Gomes, and M. Maillé (1998), Mineral aerosol production by wind erosion: Aerosol particle sizes and binding energies, *Geophys. Res. Lett.*, *25*, 991–994, doi:10.1029/98GL00502.

Alfaro, S. C., J. L. Rajot, and W. Nickling (2004), Estimation of PM20 emissions by wind erosion: Main sources of uncertainties, *Geomorphology*, *59*, 63–74, doi:10.1016/j.geomorph.2003.09.006.

Ben Mohamed, A., and J. P. Frangi (1986), Results from ground-based monitoring of spectral aerosol optical thickness and horizontal extinction: Some specific characteristics of dusty Sahelian atmospheres, *J. Clim. Appl. Meteorol.*, *25*, 1807–1815, doi:10.1175/1520-0450(1986)025<1807:RFGBMO>2.0.CO;2.

Ben Mohamed, A., J. P. Frangi, J. Fontan, and A. Druilhet (1992), Spatial and temporal variations of atmospheric turbidity and related parameters in Niger, *J. Appl. Meteorol.*, *31*, 1286–1294, doi:10.1175/1520-0450(1992)031<1286:SATVOA>2.0.CO;2.

Bielders, C. L., J. L. Rajot, and K. Michels (2004), L'érosion éolienne dans le Sahel Nigérien: Influence des pratiques culturales actuelles et méthodes de lutte, *Secheresse*, *15*(1), 19–32.

Chou, C., P. Formenti, M. Maille, P. Ausset, G. Helas, M. Harrison, and S. Osborne (2008), Size distribution, shape, and composition of mineral dust aerosols collected during the African Monsoon Multidisciplinary Analysis Special Observation Period 0: Dust and Biomass-Burning Experiment field campaign in Niger, January 2006, *J. Geophys. Res.*, *113*, D00C10, doi:10.1029/2008JD009897.

Clarke, A. D., et al. (2004), Size distributions and mixtures of dust and black carbon aerosol in Asian outflow: Physiochemistry and optical properties, *J. Geophys. Res.*, *109*, D15S09, doi:10.1029/2003JD004378.

Draxler, R. R., and G. D. Hess (1997), Description of the HYSPLIT_4 modeling system, *NOAA Tech. Memo. ERL-224*, 24 pp., Silver Spring, Md.

Dubief, J. (1979), Review of the North African climate with particular emphasis on the production of eolian dust in the Sahel zone and in the Sahara, in *Saharan Dust*, edited by C. Morales, pp. 27–48, John Wiley, Hoboken, N. J.

Engelstaedter, S. I. T., and R. Washington (2006), North African dust emissions and transport, *Earth Sci. Rev.*, *79*(1–2), 73–100, doi:10.1016/j.earscirev.2006.06.004.

Formenti, P., et al. (2008), Regional variability of the composition of mineral dust from western Africa: Results from the AMMA SOP0/DABEX and DODO field campaigns, *J. Geophys. Res.*, doi:10.1029/2008JD009903, in press.

Gaudichet, A., F. Echalar, B. Chatenet, J. P. Quisefit, G. Malingre, H. Cachier, P. Buat-Menard, P. Artaxo, and W. Maenhaut (1995), Trace elements in tropical African savanna biomass burning aerosols, *J. Atmos. Chem.*, *22*, 19–39, doi:10.1007/BF00708179.

Gomes, L., J. L. Rajot, S. C. Alfaro, and A. Gaudichet (2003), Validation of a dust production model from measurements performed in Spain and Niger, *Catena*, *52*(3–4), 257–271.

Goossens, D., and J. L. Rajot (2008), Techniques to measure the dry Aeolian deposition of dust in arid and semi-arid landscapes: A comparative study in Sahelian West Africa, *Earth Surf. Processes Landforms*, *33*, 178–195, doi:10.1002/esp.1533.

Goudie, A. S., and N. J. Middleton (2001), Saharan dust storms: Nature and consequences, *Earth Sci. Rev.*, *56*(1–4), 179–204.

Guengant, J. P., and F. Banoin (2003), *Dynamique des populations, disponibilites en terres et adaptation des regimes fonciers: Le cas du Niger*, edited by A. Quesnel, G. Gendreaus, and M. Lututala, 144 pp., Food and Agric. Org., Rome.

Haywood, J., et al. (2008), Overview of the Dust and Biomass-burning Experiment and African Monsoon Multidisciplinary Analysis special observing period-0, *J. Geophys. Res.*, doi:10.1029/2008JD010077, in press.

Heese, B., and M. Wiegner (2008), Vertical aerosol profiles from Raman polarization lidar observations during the dry season AMMA field campaign, *J. Geophys. Res.*, *113*, D00C11, doi:10.1029/2007JD009487.

Holben, B. N., et al. (2001), An emerging ground-based aerosol climatology: Aerosol optical depth from AERONET, *J. Geophys. Res.*, *106*, 12,067–12,097, doi:10.1029/2001JD900014.

Intergovernmental Panel on Climate Change (2001), *Climate Change 2001: The Scientific Basis. Third Assessment Report*, edited by J. T. Houghton et al., 944 pp., Cambridge Univ. Press, Cambridge, U.K.

Intergovernmental Panel on Climate Change (2007), *Climate Change 2007: The Physical Science Basis. Contribution of Working Group I to the Fourth Assessment. Report of the Intergovernmental Panel on Climate Change*, Cambridge Univ. Press, Cambridge, U.K.

Johnson, B. T., B. Heese, S. A. McFarlane, P. Chazette, A. Jones, and N. Bellouin (2008), Vertical distribution and radiative effects of mineral dust biomass burning aerosol over West Africa during DABEX, *J. Geophys. Res.*, *113*, D00C12, doi:10.1029/2008JD009848.

Laurent, B. (2005), Simulation des émissions d'aérosols désertiques à l'échelle continentale: Analyse climatologique des émissions du nord-est de l'Asie et du nord de l'Afrique, Ph.D. thesis, Univ. de Paris 12 Val de Marne, Creteil, France.

Leblanc, M., G. Favreau, S. Massuel, S. Tweed, M. Loireau, and B. Cappelaere (2008), Land clearance and hydrological change in the Sahel: SW Niger, *Global Planet. Change*, *61*(3–4), 135–150, doi:10.1016/j.gloplacha.2007.08.011.

Lothom, M., S. Frédérique, F. Lohou, and B. Campistron (2008), Observation of the diurnal cycle in the low troposphere of West Africa, *Mon. Weather Rev.*, doi:10.1175/2008MWR2427.1, in press.

Marticorena, B., and G. Bergametti (1995), Modeling the atmospheric dust cycle: 1. Design of a soil derived dust production scheme, *J. Geophys. Res.*, *100*, 16,415–16,430, doi:10.1029/95JD00690.

Mbourou, G. N., J. J. Bertrand, and S. E. Nicholson (1997), The diurnal and seasonal cycles of wind-borne dust over Africa north of the equator, *J. Appl. Meteorol.*, *36*, 868–882, doi:10.1175/1520-0450(1997)036<0868:TDASCO>2.0.CO;2.

Ogunjobi, K. O., Z. He, and C. Simmer (2008), Spectral aerosol optical properties from AERONET Sun-photometric measurements over West Africa, *Atmos. Res.*, *88*, 89–107, doi:10.1016/j.atmosres.2007.10.004.

Osborne, S. R., B. T. Johnson, J. M. Haywood, A. J. Baran, M. A. J. Harrison, and C. L. McConnell (2008), Physical and optical properties of mineral dust aerosol during the Dust and Biomass-burning Experiment, *J. Geophys. Res.*, *113*, D00C03, doi:10.1029/2007JD009551.

Rajot, J. L. (2001), Wind blown sediment mass budget of Sahelian village land units in Niger, *Bull. Soc. Geol. Fr.*, *172*(5), 523–531, doi:10.2113/172.5.523.

Rajot, J. L., and C. Valentin (2001), Wind eroded versus deposited mineral dust: A mass budget for a Sahelian village land unit in Niger, paper presented at International Soil Erosion Symposium, Am. Soc. of Agric. Eng., Honolulu, Hawaii.

Rajot, J. L., M. Sabre, and L. Gomes (1995), Measurement of vertical fluxes of soil-derived dust during wind erosion events in a Sahelian region (Niger), in *Wind Erosion in West Africa: The Problem and Its Control*, edited by B. Buerkert, B. E. Allison, and M. Von Oppen, pp. 49–56, Margraf, Weikersheim, Germany.

Redelsperger, J. L., C. D. Thorncroft, A. Diedhiou, T. Lebel, D. J. Parker, and J. Polcher (2006), African Monsoon Multidisciplinary Analysis: An international research project and field campaign, *Bull. Am. Meteorol. Soc.*, *87*(12), 1739–1746, doi:10.1175/BAMS-87-12-1739.

Schütz, L., R. Jaenicke, and H. Petrick (1981), Saharan dust transport over the North Atlantic Ocean, in *Desert Dust*, edited by T. L. Péwé, *Spec. Pap. Geol. Soc. Am.*, *186*, 87–100.

Slingo, A., et al. (2006), Observations of the impact of a major Saharan dust storm on the atmospheric radiation balance, *Geophys. Res. Lett.*, *33*, L24817, doi:10.1029/2006GL027869.

Sonntag, D. (1990), Important new values of the physical constants of 1986: Vapour pressure formulations based on the IST-90 and psychrometer formulae, *Z. Meteorol.*, *70*(5), 340–344.

Swap, R., M. Garstang, S. Greco, R. Talbot, and P. Kaallberg (1992), Saharan dust in the Amazon basin, *Tellus, Ser. B*, *44*(2), 133–149, doi:10.1034/j.1600-0889.1992.t01-1-00005.x.

Thomson, M. C., A. M. Molesworth, M. H. Djingarey, K. R. Yameogo, F. Belanger, and L. E. Cuevas (2006), Potential of environmental models to predict meningitis epidemics in Africa, *Trop. Med. Int. Health*, *11*(6), 781–788, doi:10.1111/j.1365-3156.2006.01630.x.

Valentin, C., J. L. Rajot, and D. Mitja (2004), Responses of soil crusting, runoff and erosion to fallowing in the sub-humid and semi-arid regions of West Africa, *Agric. Ecosyst. Environ.*, *104*, 287–302, doi:10.1016/j.agee.2004.01.035.

Washington, R., M. C. Todd, S. Engelstaedter, S. Mbainayel, and F. Mitchell (2006), Dust and the low-level circulation over the Bodélé Depression, Chad: Observations from BoDEx 2005, *J. Geophys. Res.*, *111*, D03201, doi:10.1029/2005JD006502.

S. Alfaro, B. Chatenet, S. Chevaillier, K. Desboeufs, P. Formenti, A. Gaudichet, E. Journet, B. Marticorena, and S. Triquet, Laboratoire Interuniversitaire des Systèmes Atmosphériques, Universités Paris 12 Val de Marne et Paris 7-Denis Diderot, CNRS, 61 Av. du Général de Gaulle, F-94010 Créteil, France.

A. Maman, N. Mouget, J. L. Rajot, and A. Zakou, Institut de Recherche pour le Developpement, UR 176, BP 11416 Niamey, Niger. (jeanlouis.rajot@ird.fr)